Article

Large-scale medieval urbanism traced by UAV–lidar in highland Central Asia

Michael D. Frachetti[1✉], Jack Berner[1], Xiaoyi Liu[1,2], Edward R. Henry[3], Farhod Maksudov[4] & Tao Ju[2]

Aerial light detection and ranging (lidar) has emerged as a powerful technology for mapping urban archaeological landscapes, especially where dense vegetation obscures site visibility[1,2]. More recently, uncrewed aerial vehicle/drone lidar scanning has markedly improved the resolution of three-dimensional point clouds, allowing for the detection of slight traces of structural features at centimetres of detail across large archaeological sites, a method particularly useful in areas such as mountains, where rapid deposition and erosion irregularly bury and expose archaeological remains[3]. Here we present the results of uncrewed aerial vehicle–lidar surveys in Central Asia, conducted at two recently discovered archaeological sites in southeastern Uzbekistan: Tashbulak and Tugunbulak. Situated at around 2,000–2,200 m above sea level, these sites illustrate a newly documented geography of large, high-altitude urban centres positioned along the mountainous crossroads of Asia's medieval Silk Routes (6th–11th century CE (Common Era)[4,5]. Although hidden by centuries of surface processes, our pairing of very-high-resolution surface modelling with semiautomated feature detection produces a detailed plan of monumental fortifications and architecture spanning 120 ha at Tugunbulak, thereby demonstrating one of the largest highland urban constellations in premodern Central Asia. Documentation of extensive urban infrastructure and technological production among medieval communities in Central Asia's mountains—a crucial nexus for Silk Road trade networks[6]—provides a new perspective on the participation of highland populations in the economic, political and social formation of medieval Eurasia.

Urbanism has been a central focus of archaeological research for more than a century, providing countless insights into the transformation of political, economic, technological and ideological organization of societies worldwide[7–9]. Today, concepts of urbanism are expanding to accommodate considerable variations in site scale and density, population mobility and functionality documented across premodern cities[10], giving rise to alternative models that include low-density urbanism, prestate megasites and permanent, large-scale centres with fluctuating demographics and social networks[11–16]. This wider conceptualization of urbanism includes the construction of dense population centres among (broadly defined) nomadic societies—for example, in Africa and Inner Asia, where population mobility was frequently a complement to the formation of large, permanent places rather than its antithesis[13,17,18].

Archaeology increasingly shows unique urban developments in marginal environments such as wetlands, where canonical equations between large-scale infrastructure, agricultural production and economic specialization take new forms[19]. In the past decade, airborne light detection and ranging (lidar) has revolutionized the discovery and mapping of urban centres in territories either obscured by dense vegetation or simply unexplored because of significant logistical limitations to research, namely tropical jungles[1,2,20,21]. Aerial three-dimensional photogrammetry has likewise been instrumental in mapping large population centres in the open grasslands of eastern Eurasia and Mongolia[22,23]. Nevertheless, the vast majority of premodern urban developments have been found in coastal and/or low-elevation riparian settings, documented over decades of intensive archaeological survey and excavation[24–27].

In contrast to its deep antiquity in lowland contexts, large-scale, premodern urbanism remains comparatively rare in high-mountain regions of the world. Today, less than 3% of the global population lives over 2,000 m above sea level (MASL) and only around 1% over 2,500 m, mostly found in the Andes and the Tibetan Plateau[28]. Archaeological cities documented above 2,000 MASL (for example, Machu Picchu, Tiwanaku, Cusco and Lhasa) are often seen as anomalous due to the perceived social, environmental and technological challenges posed by 'high-altitude' for large aggregated settlements: namely, limited agricultural productivity, harsh seasonality regimes, severe ruggedness and high-energy geomorphology[29–31]. At higher latitudes, significant reduction in productivity is met at even lower absolute elevation—for example, alpine tree lines are as low as 2,000–2,500 MASL at about 40° N

[1]Spatial Analysis, Interpretation & Exploration (SAIE) laboratory, Department of Anthropology, Washington University in St. Louis, St. Louis, MO, USA. [2]Department of Computer Science and Engineering, Washington University in St. Louis, St. Louis, MO, USA. [3]Department of Anthropology, Colorado State University, Fort Collins, CO, USA. [4]National Center of Archaeology, Uzbekistan Academy of Sciences, Tashkent, Uzbekistan. ✉e-mail: frachetti@wustl.edu
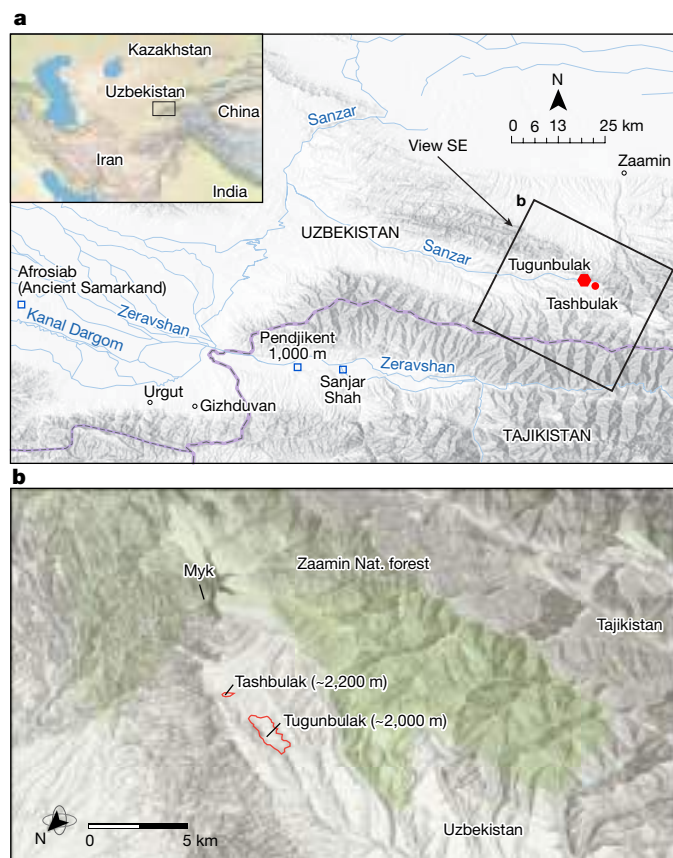
Fig. 1 | Location of study sites. a, Regional map of Central Asia (inset) and location of Tashbulak and Tugunbulak. **b**, Isometric view of topography of southeastern Uzbekistan, showing the highland context of Tugunbulak and Tashbulak. Credit: ©Open StreetMap Contributors, Tom Tom, Foursquare METI/NASA, USGS. Open Database Licence.

latitude[32]. Nevertheless, the conceptual link between highland environmental constraints and their presumed limitations for sustained, large-scale urbanism is also rooted in a considerable data bias born from a comparative lack of archaeological research in high-altitude, which restricts our potential insights concerning ecological innovation, social organization and the economic strategies of mountain societies[33]. This bias is exacerbated by the fact that periodic oscillations between high-energy erosion and rapid sedimentation, common in rugged mountain settings, can bury archaeological remains deeply or render them visually indistinguishable from the natural terrain.

Given these challenges, highland mountain settings present an ideal context for aerial reconnaissance using the latest advances in uncrewed aerial vehicle (UAV)–lidar, which is increasingly used for detailed surface mapping of discrete archaeological sites in a range of settings[21,34–36]. UAV–lidar provides resolution magnitudes higher than that achieved by previous airborne lidar platforms, largely due to its lower flight altitude than that required by larger aircraft[37–40]. Coupled with today's computational capacity to coregister large arrays of low-altitude UAV–lidar scans, the resulting composite point clouds provide both extensive and very-high-resolution (VHR) surface models with mean point spacing of 0.05–0.10 m, which allow for detailed computational analysis of large archaeological contexts using surface feature detection algorithms.

Here we present the results of UAV–lidar surveys in Central Asia, conducted at two high-altitude archaeological settings in southeastern Uzbekistan: Tashbulak and Tugunbulak. First discovered in 2011 and 2015, respectively, these sites are located at elevations roughly 2,000–2,200 MASL (Fig. 1a,b) and, together, define an interconnected

geography of high-altitude centres situated along the mountainous crossroads of Asia's medieval Silk Routes (6th–11th century CE (Common Era)[4,5]. To the naked eye, the modern surfaces of Tashbulak and Tugunbulak appear as grassy, undulating fields with large, pyramidical mounds and sparse surface ceramics as the only indicators of their archaeological character (Extended Data Fig. 1a,b). Although centuries of erosion and sedimentation have hidden these sites in plain view, the pairing of VHR surface modelling with semiautomated feature detection produces a detailed delineation of architecture and fortification spread over roughly 12 ha at Tashbulak and 120 ha at Tugunbulak, showing one of the largest and most comprehensive urban plans of any medieval city documented at or above 2,000 MASL in Central Asia.

This study also verifies the spatiostatistical correlation between predicted archaeological features automapped from the VHR surface model at Tashbulak and actual architectural remains documented there using subsurface geophysical survey and traditional archaeological excavation, building on previous approaches for paired lidar and subsurface geophysical analysis[41]. Coupling of high-resolution lidar and geophysics illustrates the vast potential of this intersectional method to accurately chart large-scale, fortified urban planning in erosional mountain environments. But far beyond the increased efficiency of reconnaissance and high-resolution mapping that VHR surface models allow, our results provide detailed mapping of both intensive and extensive urban investment in the highland regions of Central Asia—comparable in scale to contemporaneous lowland medieval cities. The fortified urban constellation evident at Tugunbulak, in particular, raises new questions concerning the political and economic function of mountain cities in shaping the medieval Silk Routes, and prompts important reconsiderations of mobility, trade and the environmental and technological resources needed to sustain extensive urban infrastructure and large populations at high-elevation more generally.

UAV–lidar and analysis of highland cities

In July 2022, the Archaeological Research of the Qarakhanids project conducted 22 low-flying UAV–lidar scans of the previously unstudied archaeological context of Tugunbulak and the recently documented site of Tashbulak[5]. Individual UAV–lidar scans captured point clouds spanning roughly 10–60 ha, collected at a mean point spacing of 0.05–0.09 m, spatially coregistered to generate composite VHR point clouds for each site. With a combined surface area of approximately 200 ha characterized by around 465 million points, these data are among the highest-resolution, large-scale, archaeological lidar models published to date (Supplementary Table 1).

The composite VHR surface model of Tugunbulak was produced from a selection of 17 coregistered point clouds spanning 158 ha, with an average of 267 points per square metre. Visualized as a hill-shaded digital terrain model (DTM) at a resolution of 2.5 cm per pixel, the lidar surface reconstruction shows four main sectors (A–D) of structural investment, including fortified mounds, extensive walls, dense architecture, roadways, structural terracing and engineering, across the full extent of analysis (Fig. 2). At Tashbulak, the VHR lidar model covered 24.4 ha with an average of 176 points per square metre, showing a central sector of dense architecture (roughly 7 ha) with fortifications and burial grounds extending over around 12 ha of the scanned area (Fig. 3).

The refined topographic resolution of these surface models allows for the effective use of semiautomated surface analysis to delineate potential archaeological features. In this context, useful geometric correlates for underlying structures are the topographic 'ridges' that signal local surface anomalies. Mathematically, a ridge on a smooth, three-dimensional surface is defined as the loci of points where the maximal principal curvature reaches a local maximum in the maximal
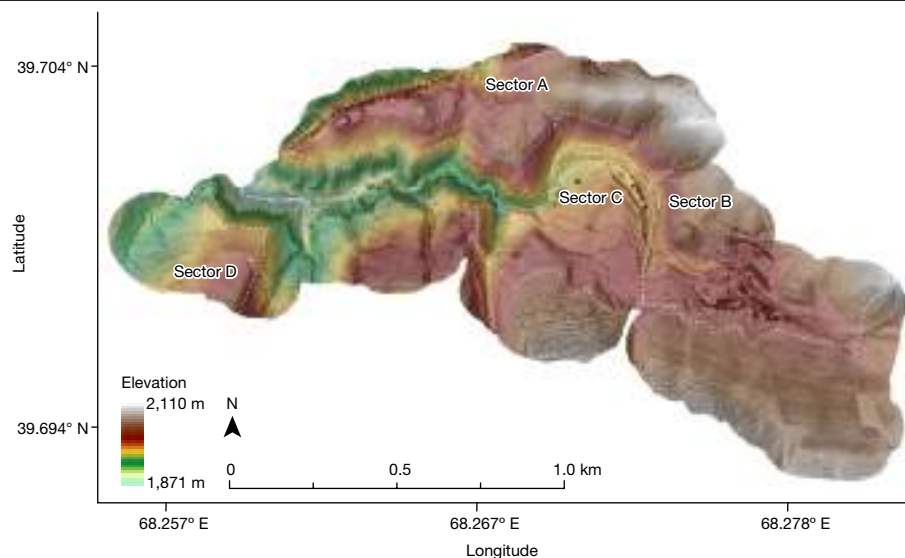
Fig. 2 | Lidar mapping of Tugunbulak. VHR lidar surface reconstruction of Tugunbulak. Visualized resolution at 2.5 cm per pixel, hill-shaded with ×2 vertical exaggeration.

curvature direction. Discrete ridge lines, represented as line segments, can be extracted from a triangular mesh using a variety of algorithms. We adopted the method of Yoshizawa et al.[42], due to its efficiency in regard to large, high-resolution meshes and robustness against noise, to produce perceptually salient ridge lines called crest lines. When applied to the VHR point cloud surfaces at Tugunbulak and Tashbulak, the crest lines effectively illustrate the sites' complex architectural planning and infrastructural layouts (Fig. 4a,b and Extended Data Fig. 2a,b). In comparison with natural topographic variations, architectural crest line features can be delineated on account of their symmetrical angular regularity and coherent repetitive structural alignments. As such,

crest lines facilitate a range of quantitative assessments of the scale, architectural layout and construction intensity of each highland centre (for example, total built area, number of structures, urban zoning and terracing) more comprehensively than visual inspection of the surface alone (discussed below).
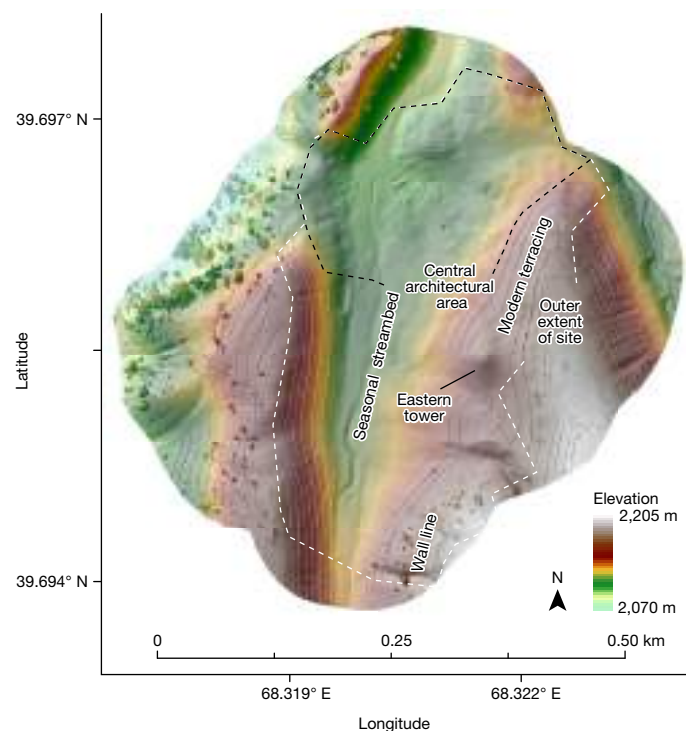
Tugunbulak sector A

At Tugunbulak, the largest area of contiguous architecture was built along an elevated ridge in the northwestern sector of the site (sector A) (Fig. 4a). Encompassing a continuous built area of around 21 ha, the crest lines in sector A highlight a dense distribution of rectilinear alignments resembling organized, multistructure architectural compounds, terracing structures and long linear berms, or walls (Fig. 4b). Sector A also contains three large, architectural mounds (Fig. 4c,d), each located on prominent elevated positions overlooking intervening structures at regular intervals (around 250 m). Three smaller mounded features are also evident on the eastern hilltops of sector A, connected by a low berm feature, potentially reflecting a sequence of ridge line watchtowers.

The detailed crest lines in sector A delineate a minimum of 300 unique structures that fall into three size classifications: small (30–70 m²), medium (70–1,000 m²) and large (1,000–4,300 m²). Topographically, many of the smaller structures appear as groupings of low depressions, forming clusters of adjacent buildings with shared walls, separated by narrow corridors or roadways. Precise volume calculations of the three largest mound features within sector A range from more than 250,000 m³ for the largest structure (A2) to 27,000 m³ for the smallest (A3), with a combined volume of 381,288 m³ (Supplementary Table 2). Even in its considerably eroded condition, the projected total volume of major fortifications and architecture in sector A indicates a monumental and prolonged investment in construction and engineering at Tugunbulak. Preliminary sampling for radiometric dating in sector A situates the site's occupation of this area from the mid-6th to the late 10th century CE (Extended Data Fig. 3 and Supplementary Table 3), although more site-wide excavation and chronological modelling is required to confirm this chronology across other sectors.
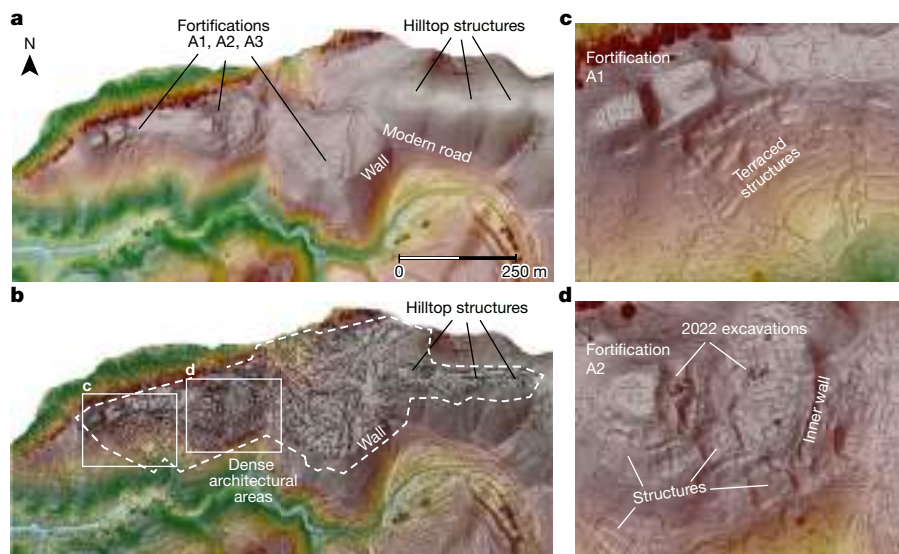
Tugunbulak sector B

The northeastern quarter of the site, sector B, is delineated by two large, rectangular mound features—probably representing collapsed fortifications built on bedrock promontories that overlook a streambed

Fig. 3 | Lidar mapping of Tashbulak. VHR lidar surface reconstruction of Tashbulak. Visualized resolution at 2.5 cm per pixel, hill-shaded with ×2 vertical exaggeration.

Fig. 4 | Lidar and crest line mapping of sector A, Tugunbulak. a–d, Details of lidar surface of sector A, Tugunbulak (hill-shaded with ×2 vertical exaggeration) (**a**), weighted crest line feature mapping of sector A (**b**), detailed topography and crest lines of fortification A1 (**c**) and detailed topography and crest lines of fortification A2 (**d**).

that divides the area into northern and southern halves (Extended Data Fig. 4a,b). Volume calculations of the two archaeological mounds in sector B are 171,000 and 91,000 m³ (Supplementary Table 2). Long rectilinear features extending from these mounds define a central area bordered on the north by steep hillsides and the streambed to the south. The detailed topography and crest lines show multiple loci of rectilinear structures and buildings, although these are less defined and continuous than in sector A on account of active occupation, animal corralling and surface modification by modern occupants. To the south of the streambed, terraced platforms with prominent rectilinear berms indicate the continuance of walls or other infrastructure, enclosing an area of approximately 23 ha.

Tugunbulak sectors C and D

Crest line analysis in the southern territory of Tugunbulak identified at least two additional areas with topographic evidence of walls, structures and terracing, designated sectors C and D. Sector C contains roughly 15.1 ha of terraced terrain, used today for cultivation of fodder crops such as alfalfa. Modern mechanized ploughing and active sedimentation in this area leave only the most robust topographic features evident in the surface model (Extended Data Fig. 5a,b). Continuous berms oriented at right angles are interpreted as wall corners, connected to an adjacent pair of low mounded features possibly indicating collapsed fortifications. In addition, the crest lines show at least two additional areas with evidence of structural architecture, which are interpreted as discrete areas of occupation within sector C.

Similar linear berms oriented at right angles and rectangular crest line alignments are evident in sector D, also interpreted as wall constructions and buildings (Extended Data Fig. 5c,d). The wall feature appears to run lengthwise (perpendicular) up the slope and turns to define an area of approximately 18 ha, within which there are small clusters of rectangular features indicating discrete structures.

The total distribution and layout of crest line features at Tugunbulak show an extensive and monumental scale of architectural investment spanning a total built area of at least 43 ha in sectors A and B, with the outer berms—interpreted as eroded walls—enclosing across a larger archaeological landscape in the order of 120–130 ha. The aggregate volume of the five large archaeological mounds, interpreted as collapse

fortifications, equals 648,330 m³. With areas encompassing around 625 m² or more, the citadel castles at Tugunbulak were fortified using dense, rammed-earth walls with surrounding structures made of stone and mudbrick architecture, based on regional analogues (for example, Kafir Kala[43]). Such building technology is archaeologically verified for the central mound A2, which had a rammed-earth wall roughly 3 m thick and densely arranged structures with robust stone foundations (Supplementary Fig. 5). Whereas future archaeological testing is required to confirm the spatial extent, range of building technology and labour investment for architecture and defensive features across the entire site (notably sectors C and D), the crest line analysis of Tugunbulak's VHR surface model illustrates in unprecedented detail the monumental scale, architectural planning and functional organization of one of the largest known high-elevation urban contexts in medieval Central Asia.

Correlation against drawn lines

To quantify the efficacy and reliability of crest line feature detection versus manual digitization at Tugunbulak, we calculated the hit-rate correlation between semiautomated crest lines and manually digitized features within a randomly selected polygon in sector A. Digitized features were identified visually from the high-resolution, hill-shaded DTM and drawn without reference to the crest lines (Methods and Extended Data Fig. 6). In our classification scheme, a true positive is defined as any crest line pixel (predicted archaeological features) that hits a manually traced line pixel within a predefined radius (for example, 1 m). We also calculated a confusion matrix to assess the spatial correlation between manually identified and crest line features, yielding user accuracies ranging from 80.8 to 94.5% and producer accuracies from 22.2 to 32.7%, depending on the search radius used.

High user accuracy is an indicator that the wall lines visually identified are nearly fully captured by the crest line algorithm, whereas low producer accuracy indicates a significant percentage of crest lines that are not evident to the human eye, even when the surface is visualized in high resolution. Because manual lines are traced based on raster resolution and hill-shade visualization, they have a higher error of omission whereas crest lines have a higher error of commission. In other words, semiautomated crest lines are statistically more complete and detailed than human-traced features, but can also contain more noise or false positives. In most cases, however, visual inspection of
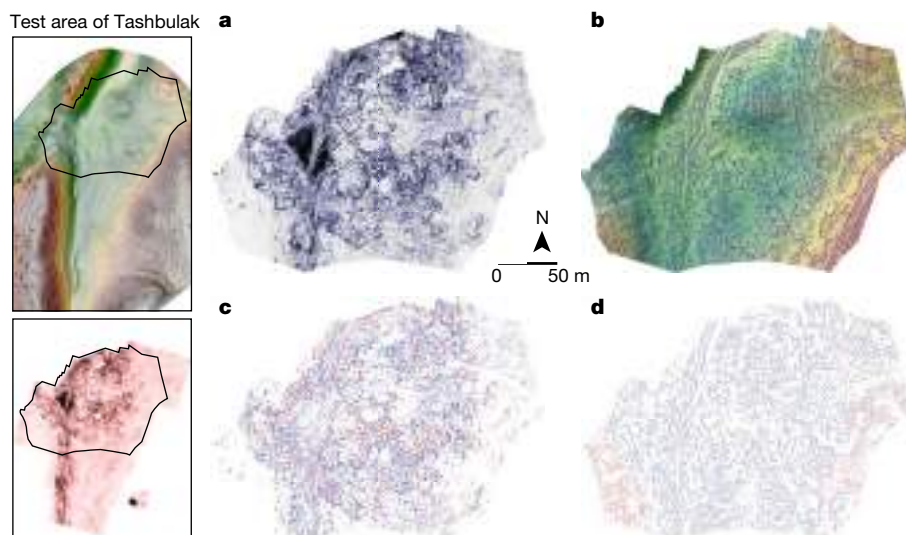
Fig. 5 | Comparison of GPR and lidar crest lines at Tashbulak. a, Centrelines (blue) derived from GPR; black lines denote confirmed subterranean architecture. **b**, Lidar crest lines (blue) over the VHR lidar surface at Tashbulak (correlation radius of 1.0 m). **c**, GPR centrelines correlated with lidar crest lines (blue denotes hits, rate 0.73; red denotes centrelines falling outside correlation radius). **d**, Lidar crest lines correlated with GPR centrelines (blue denotes hits, rate 0.79; red denotes crest lines falling outside correlation radius).

crest line output allows for a reliable segregation of topographic noise from newly identified architectural features, because archaeological features tend to have regular alignment and orientation, especially in reference to manually confirmed features. As such, visual confirmation of crest line shape and orientation is useful for determination of both true and false positives, especially when paired with manually confirmed features. To further assess the reliability of crest lines for charting actual subsurface archaeological features, we relied on data from the better archaeologically documented site of Tashbulak.

Tashbulak

Located a mere 5 km from Tugunbulak, the VHR surface model of Tashbulak spanned a total area of 24.4 ha, showing approximately 7 ha of dense architectural alignments visible in the crest line map (Extended Data Fig. 2b,c). Visual assessment shows a common urban layout for medieval towns of the region, with an elevated 'citadel' mound surrounded by an adjacent area of dense, contiguous architecture enclosed by walled fortifications[44]. The crest line map shows at least 98 visible habitations at Tashbulak, which share size, shape and layout similar to those in sector A of Tugunbulak (ranging from 30 to 70 m² each). Berms, interpreted as wall features and mounded fortifications, delineate the southern boundary of the site (Extended Data Fig. 2b,d) and, together with the main architecture, span a total site area of 12–15 ha. It is notable that the southern extent of the site was not previously recognized using traditional archaeological methods.

Crest line correlation against GPR

A test area encompassing the central cluster of architecture at Tashbulak was selected for validation of the crest lines. This area has been partially excavated and geophysically mapped using ground-penetrating radar[5] (GPR; Supplementary Fig. 1), thus offering a clear rendering of the subterranean architecture for use as an independently verified archaeological dataset to test the accuracy and reliability of crest line features derived from the VHR surface model. Because crest lines trace curvilinear features that lie roughly at the centre of topographic anomalies (including structural foundations, walls and so on), and for the purpose of obtaining an apple-to-apple comparison, we computed similar curvilinear features from the GPR rasters known as centrelines

using the algorithm of Steger[45]. Mathematically, a centreline in a greyscale image is the loci of pixels where the intensity is locally maximal along the direction of maximal curvature. Centrelines were generated independently using greyscale renderings of each stratigraphic layer of GPR images produced at Tashbulak, mapped at sequential depths from 19 to 89 cm below the surface, at intervals of roughly 10 cm (Methods). The multilayered union of GPR centrelines taken from all depths reflects a composite tracing of all subterranean features detected by GPR (that is, not terrain based) for use as an independent 'real-world' summary of the central architectural footprint of Tashbulak (Fig. 5a), which can be spatially correlated with the crest lines detected in the same area (Fig. 5b). Areas outside the central region of architecture were not included in the test, because these have not been confirmed archaeologically.

The hit-rate calculations show a strong spatial correlation between subterranean architecture traced by GPR centrelines and the semiautomated crest lines from the VHR surface model of Tashbulak (Fig. 5c,d and Methods). To quantify the spatial correspondence between GPR centrelines and autodetected crest lines, we produced a standard confusion matrix that also indicates high levels of agreement, with user accuracy ranging from 60.7 to 80.5% and producer accuracy from 72.4 to 82.5%, all with favourable F_1 statistics (0.660–0.815) depending on the spatial parameters applied (Extended Data Figs. 7 and 8a–e). Given the high rate of correlation, these results illustrate the efficacy of crest line feature detection in accurate identification of archaeological structures from VHR lidar surfaces spanning large and variously eroded and mounded surfaces.

Discussion

UAV–lidar in highland erosional settings

UAV–lidar analysis, when used in high-canopy forest settings, provides only marginally better surface characterization than standard aerial lidar[35], yet its capacity to produce VHR point clouds is considerably greater in the analysis of dynamic erosional environments with open vegetation[46,47]. In such settings, VHR surface models derived from UAV–lidar currently offer the most refined topographic characterization available for archaeological analysis and, thus, are well suited for identification by machine automated algorithms of microtopographic variations and alignments of subsurface structures[48]. Neither UAV–lidar nor

aerial lidar has been used in Central Asia for archaeological surveys, due to both political and logistical limitations, as well as to the perception that areas of low-vegetation cover can be effectively surveyed with more accessible methods such as aerial photography, three-dimensional photogrammetry or satellite remote sensing[49,50]. This study demonstrates the efficacy of UAV–lidar for VHR surface reconstructions of large-scale archaeological landscapes, and its utility in regard to semi-automated detection, mapping and classification of extensive urban infrastructure in highland mountain settings. When combined with other archaeological approaches (for example, geophysical mapping), the end result is a subsurface correlated to aerial perspective that can transform our knowledge regarding urban adaptations of premodern highland societies and their capacity for successful engineering and resiliency in environmentally restricted contexts.

Highland urbanism in Central Asia

Although large urban centres are known in Central Asia from at least 6,000 years ago, the vast majority of archaeologically documented cities are located in lowland riparian settings (less than 1,000 m above sea level)[51]. A considerably smaller number of premodern castles, fortified towns and small cities is known throughout Central Asia in lower piedmont settings (1,000–1,500 m above sea level), but large urban centres are extremely rare above 2,000 m elevation and few highland sites have been extensively excavated. Recently excavated high-elevation towns, such as Hisorak (Tajikistan)[44] and Tashbulak (this study), are among the largest highland fortified centres published to date, yet these span a mere 7 and 12 ha, respectively. As such, the detailed crest line reconstruction of Tugunbulak, illustrating concentrated architecture and fortified structures extending over a minimum of 43 ha and the wider fortified landscape spanning as much as 120 ha, currently represents the largest, high-altitude urban constellation in medieval Central Asia. By comparison, large capital cities of the 6th–11th century CE, such as Afrasiab (medieval Samarkand) or Talas, ranged from 150 to 200 ha at their apex[52], whereas many important political capitals were much smaller[53].

The dense aggregations of multistructured buildings, courtyards, plazas, pathways, monumental fortresses and defensive infrastructure mapped at both Tugunbulak and Tashbulak resonate with aspects of known medieval architectural planning in Central Asia[53,54], with a few notable deviations. The most common urban layout of the period, evident in both small and large cities in lowland settings, consists of an elevated citadel with a fortified castle or palace that overlooks a lower town, or shahristan, typically surrounded by defensive walls. This layout is reflected at Tashbulak, and appears in a modified form at Tugunbulak, which has a less common plan consisting of a string of large fortifications overlooking intervening architectural clusters, with a sequential pattern extending nearly 2 km across the northern ridge line. To the south of the central streambed, there is a vast area of terraced rectilinear platforms, walls and occupation areas creating a complex constellation of planned architectural sectors, potentially interrupted by open or unbuilt areas. For both sites, the urban plan is designed to exploit the surrounding rugged terrain, either for its natural defensive qualities or for other environmental characteristics related to activities carried out in the city itself (for example, updraught winds for smelting or metalworking). At Tashbulak, one notable deviation from lowland urban planning is the apparent lack of an extensive residential suburb (ribat). Based on the highland environmental setting and stone alignments recovered at Tashbulak (in both GPR and crest line analysis), we suggest the likelihood of shifting seasonal population dynamics in this elevated setting, such that residential quarters may have been defined by temporary structures (for example, yurts) located outside the shahristan. This hypothesis remains to be confirmed archaeologically at both sites.

In addition to their distinctive natural environmental setting and specific design, Tashbulak and Tugunbulak together reflect the intentional development of robust fortification and planned architecture in a territory with resources distinctive from those commonly found in the lowlands. Although agricultural productivity surrounding both sites is comparatively low, Tugunbulak and Tashbulak are located within a zone of rich natural pastures that today support a range of domesticated herd animals such as cattle, sheep, goats and horses. Mobile herders using these pastures as summer herding grounds would have found these major centres to be important markets for trading and selling animal stock, a valued commodity for highlanders and lowlanders alike. Nevertheless, perhaps the most valuable and particular resource associated with both Tugunbulak and Tashbulak is the ferrous geology that defines the area where they are built. Although hard to quantify, visible geological strata rich in iron ore are distributed across the entire region from Tugunbulak to Tashbulak and beyond, to the medieval castle of Myk, roughly 12 km east of Tugunbulak, where its medieval exploitation is documented[55]. If, as we hypothesize, Tashbulak and Tugunbulak were positioned to both produce and market iron (or steel), they were also both well served in terms of local fuel, being nestled within dense juniper forests that persist in the region today.

Conclusion

Our pairing of UAV–lidar with semiautomated feature analysis illustrates the high potential for high-resolution documentation of large-scale, high-altitude cities in Central Asia, showing the complex urban planning used by highland medieval polities between the 6th and 10th century CE. Until now, the highland territories of the medieval Silk Road were seen as barriers to East–West connectivity, or simply as peripheral domains of a 'nomadic' world, a traverse between lowland oases and urban hubs of trade and connectivity. On the contrary, the vast and complex urban infrastructure documented at Tugunbulak and Tashbulak forces us to reconsider the role of urbanism in so-called 'peripheral' areas where highland communities shaped unique political and economic settings during the critical centuries of Silk Road prosperity (6th–10th century CE).

Although the scale and complexity of the fortification and architecture, especially at Tugunbulak, would categorize this city as a large population centre in the region at this time, it is the city's highland geographical location that prompts us to reconsider the social, political and economic dynamics among highland populations that supported such significant urban infrastructure. The harsh seasonal climate, limited farming capacity and rugged terrain might appear as challenges to sustaining a long-term urban constellation at this altitude. However, the mountain setting of Tugunbulak and Tashbulak also provided unique opportunities, such as the potential for increased mobility and demographic interface, as well as the potential to fortify a territory that was unfamiliar to invading outsiders. By shaping large, long-lived cities beyond the riparian zones of agricultural production, the highland communities of Tashbulak and Tugunbulak defined a new enclave in the political and economic landscape of the wider region, and ongoing work will continue to provide new insights concerning their innovations in architecture, water and land use, and ideological change in the high-altitude context of Central Asia[44,56,57]. Future exploration of mountain zones, both terrestrial and aerial, will inevitably revise our biases and expectations concerning the enduring impact of highland political entities throughout this critical historical period of East–West communication and exchange.

Online content

Any methods, additional references, Nature Portfolio reporting summaries, source data, extended data, supplementary information, acknowledgements, peer review information; details of author contributions and competing interests; and statements of data and code availability are available at https://doi.org/10.1038/s41586-024-08086-5.

Article

1. Chase, A. F., Chase, D. Z., Fisher, C. T., Leisz, S. J. & Weishampel, J. F. Geospatial revolution and remote sensing LiDAR in Mesoamerican archaeology. *Proc. Natl Acad. Sci. USA* **109**, 12916–12921 (2012).

2. Prümers, H., Betancourt, C. J., Iriarte, J., Robinson, M. & Schaich, M. Lidar reveals pre-Hispanic low-density urbanism in the Bolivian Amazon. *Nature* **606**, 325–328 (2022).

3. Casana, J. et al. Exploring archaeological landscapes using drone-acquired lidar: case studies from Hawaiʻi, Colorado, and New Hampshire, USA. *J. Archaeol. Sci. Rep.* **39**, 103133 (2021).

4. Frachetti, M. D. & Maksudov, F. The landscape of ancient mobile pastoralism in the highlands of southeastern Uzbekistan, 2000 BC – 1400 AD. *J. Field Archaeol.* **39**, 195–212 (2014).

5. Maksudov, F. et al. in *Urban Cultures in Central Asia from the Bronze Age to the Karakhanids* (eds Baumer, C. & Novák, M.) 283–305 (Harrassowitz Verlag, 2019).

6. Frachetti, M. D., Smith, C. E., Traub, C. & Williams, T. Nomadic ecology shaped the highland geography of Asia's Silk Roads. *Nature* **543**, 193–198 (2017).

7. Cowgill, G. L. Origins and development of urbanism: archaeological perspectives. *Annu. Rev. Anthropol.* **33**, 525–549 (2004).

8. Smith, M. L. The archaeology of urban landscapes. *Annu. Rev. Anthropol.* **43**, 307–323 (2014).

9. Smith, M. *Urban Life in the Distant Past: The Prehistory of Energized Crowding* (Cambridge Univ. Press, 2023).

10. Fletcher, R. Urban labels and settlement trajectories. *J. Urban Archaeol.* **1**, 31–48 (2020).

11. Nebbia, M. *Early Cities or Large Villages? Settlement Dynamics in the Trypillia Group, Ukraine*. Doctoral thesis, Durham Univ. (2017).

12. Chapman, J., Gaydarska, B. & Nebbia, M. The origins of Trypillia megasites. *Front. Digit. Humanit.* **6**, 10 (2019).

13. White, K. & Fletcher, R. Anomalous giants: form, operation, differences, and outcomes. *J. Urban Archaeol.* **7**, 275–311 (2023).

14. Bellina, B. Maritime Silk Roads' ornament industries: socio-political practices and cultural transfers in the South China Sea. *Camb. Archaeol. J.* **24**, 345–377 (2014).

15. Fletcher, R. Trajectories to low-density settlements past and present: paradox and outcomes. *Front. Digit. Humanit.* **6**, 14 (2019).

16. Miksic, J. Khao Sam Kaeo: an early port-city between the Indian Ocean and the South China Sea edited by Berenice Bellina. *J. Malays. Branch R. Asiat. Soc.* **91**, 155–159 (2018).

17. Rogers, J. D., Ulambayar, E. & Gallon, M. Urban centres and the emergence of empires in Eastern Inner Asia. *Antiquity* **79**, 801–818 (2005).

18. Honeychurch, W. & Amartuvshin, C. Hinterlands, urban centers, and mobile settings: the 'New' Old World archaeology from the Eurasian Steppe. *Asian Perspect.* **46**, 36–64 (2007).

19. Hammer, E. Multi-centric, marsh-based urbanism at the early Mesopotamian city of Lagash (Tell al-Hiba, Iraq). *J. Anthropol. Archaeol.* **68**, 101458 (2022).

20. Evans, D. H. et al. Uncovering archaeological landscapes at Angkor using lidar. *Proc. Natl Acad. Sci. USA* **110**, 12595–12600 (2013).

21. Hare, T., Masson, M. & Russell, B. High-density LiDAR mapping of the ancient city of Mayapán. *Remote Sens.* **6**, 9064–9085 (2014).

22. Reichert, S., Erdene-Ochir, N.-O., Linzen, S., Munkhbayar, Lkh & Bemmann, J. Overlooked—enigmatic—underrated: the city Khar Khul Khaany Balgas in the heartland of the Mongol world empire. *J. Field Archaeol.* **47**, 397–420 (2022).

23. Piezonka, H. et al. Lost cities in the Steppe: investigating an enigmatic site type in early modern Mongolia. *Antiquity* **97**, e12 (2023).

24. McIntosh, R. J. *Ancient Middle Niger: Urbanism and the Self-Organizing Landscape* (Cambridge Univ. Press, 2005).

25. Fletcher, R. & Evans, D. in *Old Myths and New Approaches* (ed. Haendel, A.) 42–62 (Monash Univ. Publishing, 2012).

26. Flad, R. K. & Chen, P. *Ancient Central China* (Cambridge Univ. Press, 2013).

27. Canuto, M. A. & Auld-Thomas, L. Taking the high ground: a model for lowland Maya settlement patterns. *J. Anthropol. Archaeol.* **64**, 101349 (2021).

28. Tremblay, J. C. & Ainslie, P. N. Global and country-level estimates of human population at high altitude. *Proc. Natl Acad. Sci. USA* **118**, e2102463118 (2021).

29. Aldenderfer, M. Modelling plateau peoples: the early human use of the world's high plateaux. *World Archaeol.* **38**, 357–370 (2006).

30. Janusek, J. W. Incipient urbanism at the Early Andean center of Khonkho Wankane, Bolivia. *J. Field Archaeol.* **40**, 127–143 (2015).

31. Leadbetter, M. P. & Sastrawan, W. J. Do mountains kill states? Exploring the diversity of Southeast Asian highland communities. *J. Glob. Hist.* **19**, 195–220 (2024).

32. Körner, C. in *Alpine Plant Life: Functional Plant Ecology of High Mountain Ecosystems* (ed. Körner, C.) 23–51 (Springer International Publishing, 2021).

33. Aldenderfer, M. S. in *The Handbook of South American Archaeology* (eds Silverman, H. & Isbell, W. H.) 131–143 (Springer New York, 2008).

34. VanValkenburgh, P. et al. Lasers without lost cities: using drone Lidar to capture architectural complexity at Kuelap, Amazonas, Peru. *J. Field Archaeol.* **45**, S75–S88 (2020).

35. Risbøl, O. & Gustavsen, L. LiDAR from drones employed for mapping archaeology–potential, benefits and challenges. *Archaeol. Prospect.* **25**, 329–338 (2018).

36. Li, Z. New opportunities for archaeological research in the Greater Ghingan Range, China: application of UAV LiDAR in the archaeological survey of the Shenshan Mountain. *J. Archaeol. Sci. Rep.* **51**, 104182 (2023).

37. Evans, D. Airborne laser scanning as a method for exploring long-term socio-ecological dynamics in Cambodia. *J. Archaeol. Sci.* **74**, 164–175 (2016).

38. Masini, N. et al. Medieval archaeology under the canopy with LiDAR. The (re)discovery of a medieval fortified settlement in southern Italy. *Remote Sens.* **10**, 1598 (2018).

39. Inomata, T. et al. Origins and spread of formal ceremonial complexes in the Olmec and Maya regions revealed by airborne lidar. *Nat. Hum. Behav.* **5**, 1487–1501 (2021).

40. Casana, J. et al. Multi-sensor drone survey of ancestral agricultural landscapes at Picuris Pueblo, New Mexico. *J. Archaeol. Sci.* **157**, 105837 (2023).

41. Henry, E. R., Shields, C. R. & Kidder, T. R. Mapping the Adena-Hopewell landscape in the Middle Ohio Valley, USA: multi-scalar approaches to LiDAR-derived imagery from central Kentucky. *J. Archaeol. Method Theory* **26**, 1513–1555 (2019).

42. Yoshizawa, S., Belyaev, A. & Seidel, H.-P. Fast and robust detection of crest lines on meshes. In *Proc. 2005 ACM Symposium on Solid and Physical Modeling* (eds Yoshizawa, S. et al.) 227–232 (Association for Computing Machinery, 2005).

43. Mantellini, S. & Berdimuradov, A. Archaeological explorations in the Sogdian fortress of Kafir Kala. *Anc. Civiliz. Scythia Sib.* **11**, 107–132 (2005).

44. Lurje, P. B. in *Urban Cultures of Central Asia from the Bronze Age to the Karakhanids* (eds Baumer, C. & Novák, M.) 333–348 (Harrassowitz Verlag, 2019).

45. Steger, C. An unbiased detector of curvilinear structures. *IEEE Trans. Pattern Anal. Mach. Intell.* **20**, 113–125 (1998).

46. Mayr, A., Bremer, M., Rutzinger, M. & Geitner, C. Unmanned aerial vehicle laser scanning for erosion monitoring in alpine grassland. *ISPRS Ann. Photogramm. Remote Sens. Spat. Inf. Sci.* **4**, 405–412 (2019).

47. Resop, J. P., Lehmann, L. & Hession, W. C. Drone laser scanning for modeling riverscape topography and vegetation: comparison with traditional aerial lidar. *Drones* **3**, 35 (2019).

48. Williams, P. R., Londono, A. C. & Hart, M. in *New Geospatial Approaches to the Anthropological Sciences* (eds Anemone, R. L. & Conroy, G. C.) Ch. 10 (SAR, 2018).

49. Oczipka, M. et al. Small drones for geo-archaeology in the steppes: locating and documenting the archaeological heritage of the Orkhon Valley in Mongolia. In *Remote Sensing for Environmental Monitoring, GIS Applications, and Geology IX* Vol. 7478, 747806 (SPIE, 2009).

50. Block-Berlitz, M. et al. Area-optimized, rapid UAV-borne recording of medieval heritage in Central Asia. *J. Field Archaeol.* **47**, 90–104 (2022).

51. Baipakov, K. M. *Drevnjaja i srednevekovaja urbanizacija Kazahstana (po materialam issledovanij Juzhno-Kazahstanskoj kompleksnoj arheologicheskoj jekspedicii), Kniga I. Urbanizacija v jepohu bronzy – rannem srednevekov'e* [Russian] (Inst. Archaeology MON RK, Almaty, 2012).

52. Rapin, C. in *Zwischen Ost und West. Neue Forschungen zum antiken Zentralasien* (eds Lindström, G. et al.) Vol. 14 43–82 (Philipp von Zabern, 2013).

53. Grenet, F. in *The History and Culture of Iran and Central Asia: From the Pre-Islamic to the Islamic Period* (eds Tor, D. G. & Inaba, M.) 11–40 (University of Notre Dame Press, 2022).

54. Mantellini, S., Di Cugno, G., Dimartino, R. & Berdimuradov, A. E. Change and continuity in the Samarkand oasis: evidence for the Islamic conquest from the citadel of Kafir Kala. *J. Inn. Asian Art Archaeol.* **7**, 227–253 (2016).

55. Sverchkov, L. M. A history of research on ancient mining in Uzbekistan. *Archaologische Mitteilungen Aus Iran Turan* **41**, 141–164 (2009).

56. Spengler, R. N. et al. Arboreal crops on the medieval Silk Road: Archaeobotanical studies at Tashbulak. *PLoS ONE* **13**, e0201409 (2018).

57. Bullion, E., Maksudov, F., Henry, E. R., Merkle, A. & Frachetti, M. Community practice and religion at an Early Islamic cemetery in highland Central Asia. *Antiquity* **96**, 628–645 (2022).

Methods

Lidar collection

Using a DJI Matrice 600 Pro drone equipped with base-mounted GeoSLAM Zeb Horizon lidar unit, a total of 22 UAV–lidar flights were conducted between 5 and 22 June 2022 over Tugunbulak and surrounding areas, covering a total area of 158 ha. One flight was conducted over Tashbulak covering a total scanned area of 24.4 ha. Each of these flights was conducted in favourable weather conditions at sensor altitude 25–50 m (depending on terrain). The lidar sensor emits a 903 nm laser pulse at 937 points per scan line and 160 lines per second (16 lines at 10 HZ each), with a horizontal and angular resolution of 0.2 and 2.0°, respectively (regardless of deployment platform). For the purposes of georeferencing, a total of 14 ground control points (two visible targets and 12 geolocated trench corners) were placed in the study area, and registered using a Trimble R3 GPS unit with 0.05 cm horizontal and vertical error.

Lidar processing

For Tugunbulak, a central point cloud with 14 ground control points was georeferenced (using CloudCompare v.2.12.4), with an average residual error of 0.038 m. It was then coregistered with 12 separate lidar scans covering the remainder of the site, using a combination of point-pairs picking and iterative closest-point registration[58]. The resulting composite point cloud was cleaned of anomalies and obvious errors caused at the time of data collection (for example, dust clouds), and during point cloud registration using manual selection and deletion. The resulting composite point cloud for Tugunbulak consisted of 421,512,525 points, saved in .las format. Tashbulak is entirely contained by one scan of 42,961,283 points, which was georeferenced using datum points previously recorded with a Trimble GeoExplorer 6000 GPS unit with a postprocessed horizontal error of 1 cm. We calculated the number of points per square metre and mean point spacing values for each site using the area and points totals reported above (Supplementary Table 1). To generate a high-resolution DTM for visual identification, modelling and geometric processing purposes, we converted both LAS datasets to elevation rasters in ArcGIS Pro 3.0 with 0.025 m cell size using the LAS dataset to raster function. Parameter selections included binned interpolation, mean cell assignment, yes to void filling and z-factor = 1 (see https://pro.arcgis.com/en/pro-app/latest/help/analysis/raster-functions/las-to-raster-function.htm for tool details). The resulting DTMs were then rendered as a multidirectional hill-shade map with a z-scale factor of 2 for improved visual acuity. Final visualization included an additional hill-shade layer generated using the sky view factor in Relief Visualization Toolbox software. For Tugunbulak, an arbitrary 50×50 m² grid was drawn over the hill-shaded DTM to ensure a consistent selection area for testing crest lines against visually traced features (Extended Data Fig. 6). All apparent archaeological features within one random 5,000 m² area in the residential core of the site were manually traced in ArcGIS Pro.

GPR collection at Tashbulak

Ground-penetrating radar data were collected in June 2015 using a GSSI, Inc. SIR-3000 control unit and a 400 MHz shielded antenna with an attached survey wheel. Using this configuration, we surveyed 6.5 ha of Tashbulak using an arbitrary grid-based system (60×40 m²) using zig-zag-collected transects spaced 50 cm apart. GPR radargrams were collected at 25 scans per metre and digitized to 512 samples per scan with a time window of 38 ns. These settings resulted in a maximum depth penetration of roughly 1.8 m below surface for the GPR signal. GPR data were processed using the v.7.0 MT software package (Screening Eagle Technologies). The processing workflows included conversion of GSSI, Inc. data into a format used by GPR-Slice. During this conversion we corrected the time 0 reflection in the GPR trace signal (for example, initial ground surface reflection) across the dataset

and reduced dc-drift, also known as signal wobble. The gain was then increased on all radargrams used to create our volumetric survey block to show variable reflections at depths at which the GPR trace signal was weakened due to differences in signal gain during collection, as well as to demonstrate changes in stratigraphy and soil moisture in the subsurface. A background-removal filter was then applied to remove banding from variations in the radargrams caused by moisture differences in the subsurface. We also gridded the survey area without this filter to ensure that our background-filtered data were not removing real features (for example, walls) that ran parallel to our survey lines (for example, direction of radargram collection). Finally, we used a hyperbola search on several radargrams distributed across our survey area to estimate the nanosecond-to-depth ratio based on differential hyperbola shapes in our radargrams. Data were then gridded into amplitude slice maps of the survey area, approximately 10 cm thick. Amplitude slice maps can be thought of as a horizontal slice of the survey area at a particular depth below the surface. We georeferenced each exported amplitude slice map to three data from 2015. These data were tied to real-world coordinates using a Trimble GeoExplorer 6000 series hand-held GPS logger attached to a Trimble Zephyr external antenna on a 2-m-tall ranging pole. Data were recorded for more than 2 h in each location. The GPS coordinates of data collected in the field were later postprocessed to a horizontal accuracy of 1 cm or above. Each slice was then exported to a GIS environment for further analysis and interpretation. All amplitude slice maps were georeferenced in ArcMap using a first-order polynomial transformation, resulting in root-mean square error of roughly 5 cm across the GPR datasets. A combination of multiple slice maps of our GPR results provides a composite rendering of the subterranean architecture and features at Tashbulak (Supplementary Fig. 1). Note that the area of the necropolis was not detectable using GPR, but was tested and verified using other geophysical (for example, magnetometry) and archaeological methods[57].

Volumetric calculations

Our volume calculations followed the methodology outlined in ref. 2, with slight modifications. First, the boundaries of mounds in sectors A and B were manually delineated using the DTM visualized as a hill-shaded map and a slope map. Polygons drawn over these mounds were then converted into raster layers with basal elevation values equal to the lowest points in each respective mound. Using a raster calculator, we measured the differences in elevation between each DTM pixel and the base raster, multiplied those values by DTM cell size (0.025 m) and summed all cells using zonal statistics. The combined volume of the five large mounds at Tugunbulak is equal to 648,330 m³.

Surface reconstruction from VHR point clouds and crest line feature extraction

A triangular surface mesh is reconstructed from the georeferenced composite point cloud using the screened Poisson reconstruction method[59] (as implemented in MeshLab by Cignoni et al.[60]). This method extracts the mesh on an adaptive octree grid. Maximum octree depth, which is the only parameter in the method, controls the size and resolution of the output mesh (higher depth leads to larger and finer meshes). We set the maximum depth (d) to 11 for the Tashbulak site and 13 for the Tugunbulak site, because the latter covers a significantly larger area. The reconstructed mesh contains 786,122 and 46,999,222 triangles, respectively, for the two sites. Note that the triangular meshes are reconstructed with consistent triangle normals oriented towards the 'free space' (that is, towards the sky). As a result, the features that we consider crest lines (as the loci of the maximum curvature extrema along the maximum principal direction) correspond to the upward ridges on the surface.

We extracted crest lines from the triangular mesh using the algorithm of Yoshizawa et al.[42]. This algorithm has one parameter that controls the size (in number of triangles) of the neighbourhood (n) around each

mesh vertex used to compute the principal curvatures. Smaller neighbourhoods can better capture high-frequency details (for example, small bumps on the ground), whereas larger neighbourhoods are more robust against noise. After experimenting with different neighbourhood sizes, we found that a neighbourhood size of 4 for Tashbulak and 6 for Tugunbulak best capture the architectural structures while avoiding excessive noise. As an example, Supplementary Fig. 2 shows the crest lines computed at three different neighbourhood sizes (4, 6 and 8) and mesh depths for two small regions in Tugunbulak. Note that crest lines at neighbourhood size 6 manage to preserve most of the archaeological features at neighbourhood size 4, but with much less noise, whereas a more significant loss of archaeological features can be observed at size 8.

Owing to the large size of the Tugunbulak mesh, we partitioned this into seven regions where each contains between 4,281,844 and 10,119,200 triangles. We then ran the crest line algorithm on each region independently and combined the resulting crest lines afterwards.

Spatial correlation

To compute the correlation between crest lines and visually identified, hand-traced features at Tugunbulak, we first converted each set of lines into a bitmap image by projecting them orthographically to the ground plane and rasterizing the projected lines. We utilize two separate metrics to quantify the correlation; our first method is a hit-rate calculation. For each pixel on crest lines, we search within a centred square detector, scaled according to a real-world metric (distances ranging from 0.08 to 1.4 m) (Extended Data Fig. 6). These distances represent a minimum and maximum half-width of stone wall foundations documented archaeologically at Tugunbulak (Supplementary Information) and the nearby site of Tashbulak[5]. If any pixel on the hand-drawn line falls inside this detector, we record a hit. We repeat this process with the roles of crest lines and hand-drawn lines reversed. The second method is a binary confusion matrix, standardized for remote-sensing validation[61]. In this approach, we dilate the crest lines and hand-drawn lines by convolving the initial bitmap images with the same square detector range used for hit-rate calculation. We also report the F_1 score, as a measure of precision and recall in binary classifications. Owing to the imbalanced nature of the dataset (that is, small architectural walls within an otherwise very large landscape), the F_1 score is a suitable metric of predictive performance (for reviews of these metrics in similar data environments, see refs. 62–64):

$$F_1 \text{ score} = \frac{TP}{TP + 1/2(FP + FN)}$$

where TP is the number of true positives, FP is the number of false positives and FN is the number of false negatives. The correlation statistics between crest lines and GPR centrelines at Tashbulak are computed using the same approaches, with one key difference. Because GPR images do not correspond to a simple orthographic projection of the terrain, we first need to establish a spatial correspondence between the reconstructed three-dimensional surface mesh (from which the crest lines are generated) and the raster GPR images. This process is informally known as rubber-sheeting, which we accomplish using a combination of semiautomated algorithms and user intervention as explained below.

We start by manual selection of pairs of landmarks, each consisting of a pixel location in the GPR image and a corresponding vertex on the three-dimensional surface mesh. These are selected according to visual inspection of major visible features in both datasets. To avoid compromising the accuracy of correlation between crest lines and GPR centrelines, we intentionally hid the crest lines on the surface mesh and the centrelines in the GPR image when making the selections. The landmarks are therefore selected based on visual examination of the similarity between the intensity in GPR images and terrain

features on the three-dimensional surface mesh. A total of 16 pairs of landmarks were selected, as shown in Supplementary Fig. 3a,b. We then orthographically project the three-dimensional surface mesh (with the landmarks) onto the plane, followed by manual translation and rotation to align roughly with the GPR image. At this point, the landmarks on the projected mesh are close to their corresponding landmarks on the GPR image but they do not coincide, as shown in Supplementary Fig. 3e for one of the landmark pairs (blue dot denotes the landmark on the mesh, and the red dot the corresponding landmark on the GPR image). Finally, we deform the projected triangular mesh so that each mesh landmark is moved to its corresponding GPR landmark. For a smooth deformation, the shape of the triangles should be preserved as much as possible. In particular, no triangle should be 'flipped' in the process otherwise an invalid mesh will be created. To this end, we adopt the recent deformation algorithm of Du et al.[65]. Given a triangular mesh, a subset of its vertices as 'handles' and their prescribed target locations, this algorithm computes a smooth deformation of the mesh that moves each handle to its precise target location without producing any flipped triangles. We run the algorithm by setting the handles and targets, respectively, as the mesh and GPR landmarks. Supplementary Fig. 3 shows the deformed mesh around the pair of landmarks using this algorithm. The rubber-sheeting process also carries the crest lines computed on the original three-dimensional surface mesh to the projected and deformed planar mesh (blue and red lines in Supplementary Fig. 3). We then compute the correlation between these crest lines and the GPR centrelines, in the same way as that used for correlation with hand-traced features in Tugunbulak.

The rubber-sheeting process improves alignment between the GPR centrelines and surface crest lines compared with simple orthographic projection. Supplementary Fig. 3 visually compares both sets of crest lines, those being projected orthographically (in blue) and those following deformation of the mesh, using Du et al. (in red). Observe that the latter set is closer to structural features in GPR, particularly around the landmarks (a close-up is provided in Supplementary Fig. 3d). Correlation statistics also improved (albeit slightly) with the use of mesh deformation, as shown in Supplementary Table 4. This minor improvement indicates that the terrain at Tashbulak is relatively flat, and hence the map between GPR and the terrain surface is nearly orthographic. We expect to see a greater difference between rubber-sheeting and orthographic projection for sites with more undulating terrain topography.

Processing crest lines as vectors

For quantification of architectural metrics, filtering for noise and visual illustration of weighted crest line data, crest lines were converted into Shapefile format (.shp) line segments with UTM 42 N projection. The Shapefiles were then imported into ArcGIS pro, in which we used the Unsplit Lines tool to quantify line lengths and create continuous features—that is, join polyline segments with shared nodes. For removal of non-architectural noise and improvement in visualization and data management of crest lines, we then reused the Remove Small Lines tool to screen out stand-alone segments under 1.5 m, with a maximum angle tolerance of 10°. We then repeated the Unsplit Lines process to reduce the total number of features and conjoin line segments with shared nodes into longer features.

Inclusion and ethics statement

All collaborators in this study fulfil the criteria for authorship required by Nature Portfolio journals and have been included as authors, because their participation was essential for the design and implementation of the study. Roles and responsibilities were agreed among collaborators ahead of the research. This work includes locally relevant findings, which were determined in collaboration with local partners. This research was neither severely restricted nor prohibited in the setting of the researchers, and does not result in stigmatization, incrimination, discrimination or personal risk to participants. Local and regional

research relevant to our study was taken into account in citations. All required local-, regional- and national-level permits were obtained in advance of data collection.

Reporting summary

Further information on research design is available in the Nature Portfolio Reporting Summary linked to this article.

Data availability

All relevant data are provided with the paper and its Supplementary Information. The datasets used to calibrate all radiocarbon dates are available in Supplementary Table 3. An abridged lidar dataset required to execute crest line analysis and correlation and validation analyses is openly available at GitHub (https://github.com/JasonLiu2024/high-resolution-lidar-traces-large-scale-medieval-urbanism).

Code availability

All code required to execute crest line analysis and correlation and validation analyses is openly available at GitHub (https://github.com/JasonLiu2024/high-resolution-lidar-traces-large-scale-medieval-urbanism).

58. Besl, P. J. & McKay, N. D. Method for registration of 3-D shapes. In *Sensor Fusion IV: Control Paradigms and Data Structures* (ed. Schenker, P. S.) Vol. 1611, 586–606 (SPIE, 1992).
59. Kazhdan, M. & Hoppe, H. Screened Poisson surface reconstruction. *ACM Trans. Graph.* **32**, 3 (2013).
60. Cignoni, P. et al. Meshlab: an open-source mesh processing tool. *Computing* **1**, 129–136 (2008).
61. Story, M. & Congalton, R. G. Accuracy assessment: a user's perspective. *Photogramm. Eng. Remote Sens.* **52**, 397–399 (1986).
62. Abdollahi, A., Pradhan, B., Shukla, N., Chakraborty, S. & Alamri, A. Deep learning approaches applied to remote sensing datasets for road extraction: a state-of-the-art review. *Remote Sens.* **12**, 1444 (2020).
63. Dong, R., Pan, X. & Li, F. DenseU-net-based semantic segmentation of small objects in urban remote sensing images. *IEEE Access* **7**, 65347–65356 (2019).
64. Monna, F. et al. Machine learning for rapid mapping of archaeological structures made of dry stones–example of burial monuments from the Khirgisuur culture, Mongolia. *J. Cult. Herit.* **43**, 118–128 (2020).
65. Du, X. et al. Isometric energies for recovering injectivity in constrained mapping. In *SIGGRAPH Asia 2022 Conference Papers* 1–9 (ACM, 2022).

Author contributions M.D.F. and F.M. conceptualized the study. M.D.F., F.M. and E.R.H. collected the data. M.D.F. and T.J. designed the methodology and analysis, with input from F.M., J.B. and X.L. M.D.F., J.B., X.L., E.R.H. and T.J. carried out the analysis. M.D.F. and J.B. wrote the initial draft, and all authors contributed to writing and editing of the final manuscript.
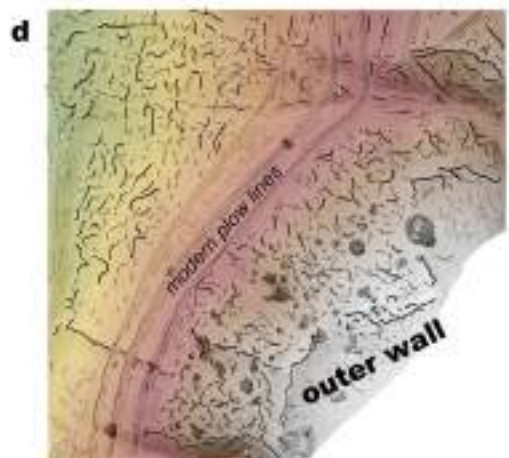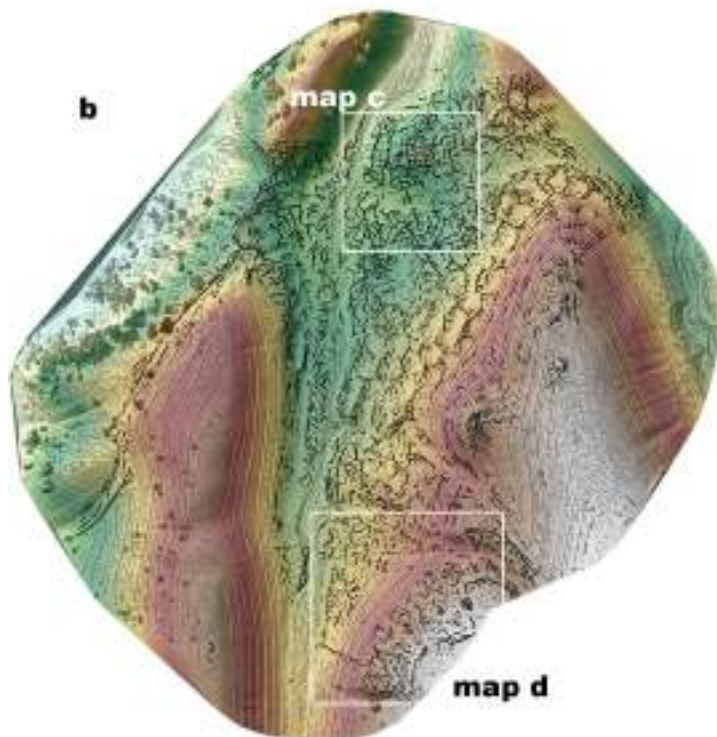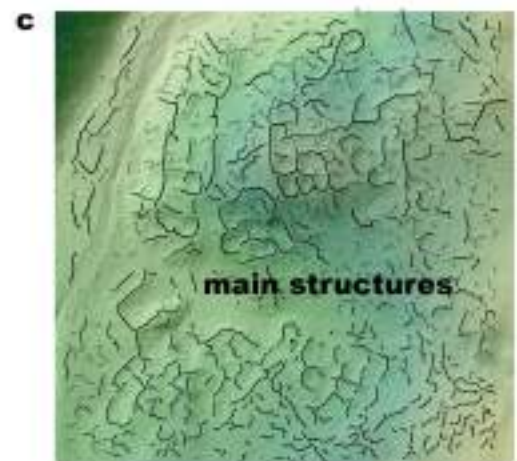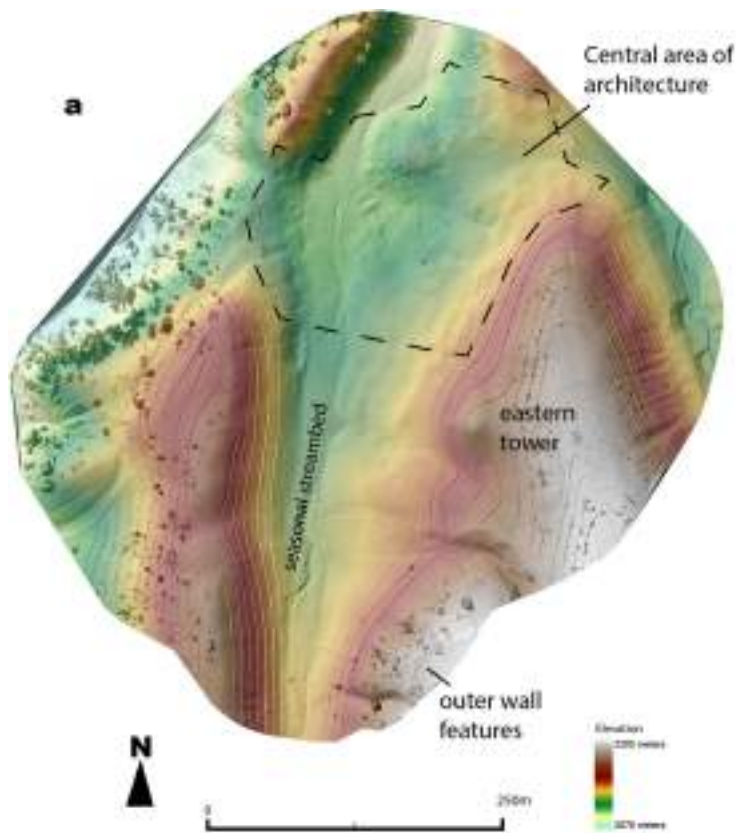
Extended Data Fig. 1 | Panoramic photos of study sites. a) Tugunbulak, view east and b) Tashbulak, view northeast. Photos by M. Frachetti.
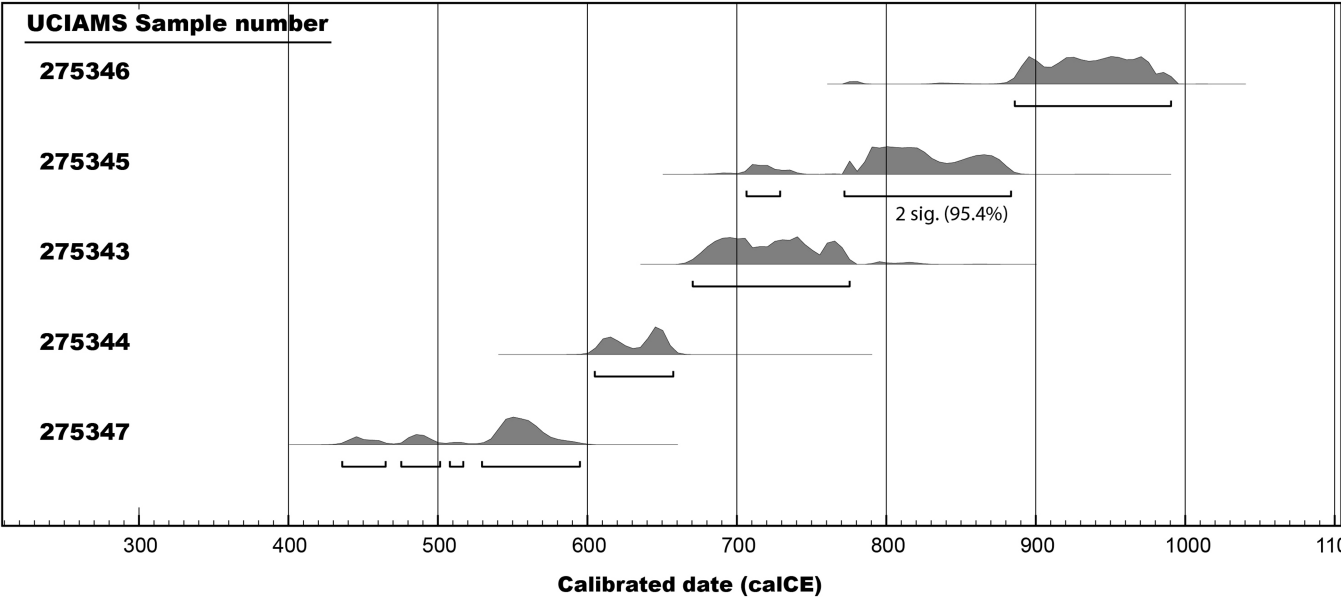
Extended Data Fig. 2 | Detail lidar and crestline mapping, Tashbulak. a) Very high resolution (VHR) lidar surface of Tashbulak, hill-shaded with 2x vertical exaggeration; b) Weighted crest line feature mapping of Tashbulak; c) detail of main structural area (hill shaded topography with crest lines); d) detail of southern extent of site showing outer wall features (hill shaded topography with crest lines).

OxCal v4.4.4 Bronk Ramsey (2021); r:5 Atmospheric data from Reimer et al (2020)

Extended Data Fig. 3 | Radiocarbon chronology, Tugunbulak. Preliminary calibrated date ranges of AMS radiocarbon samples from Tugunbulak (sector A, excavations 2022). (For dates and calibration data, see Supplementary Information, Table 3).
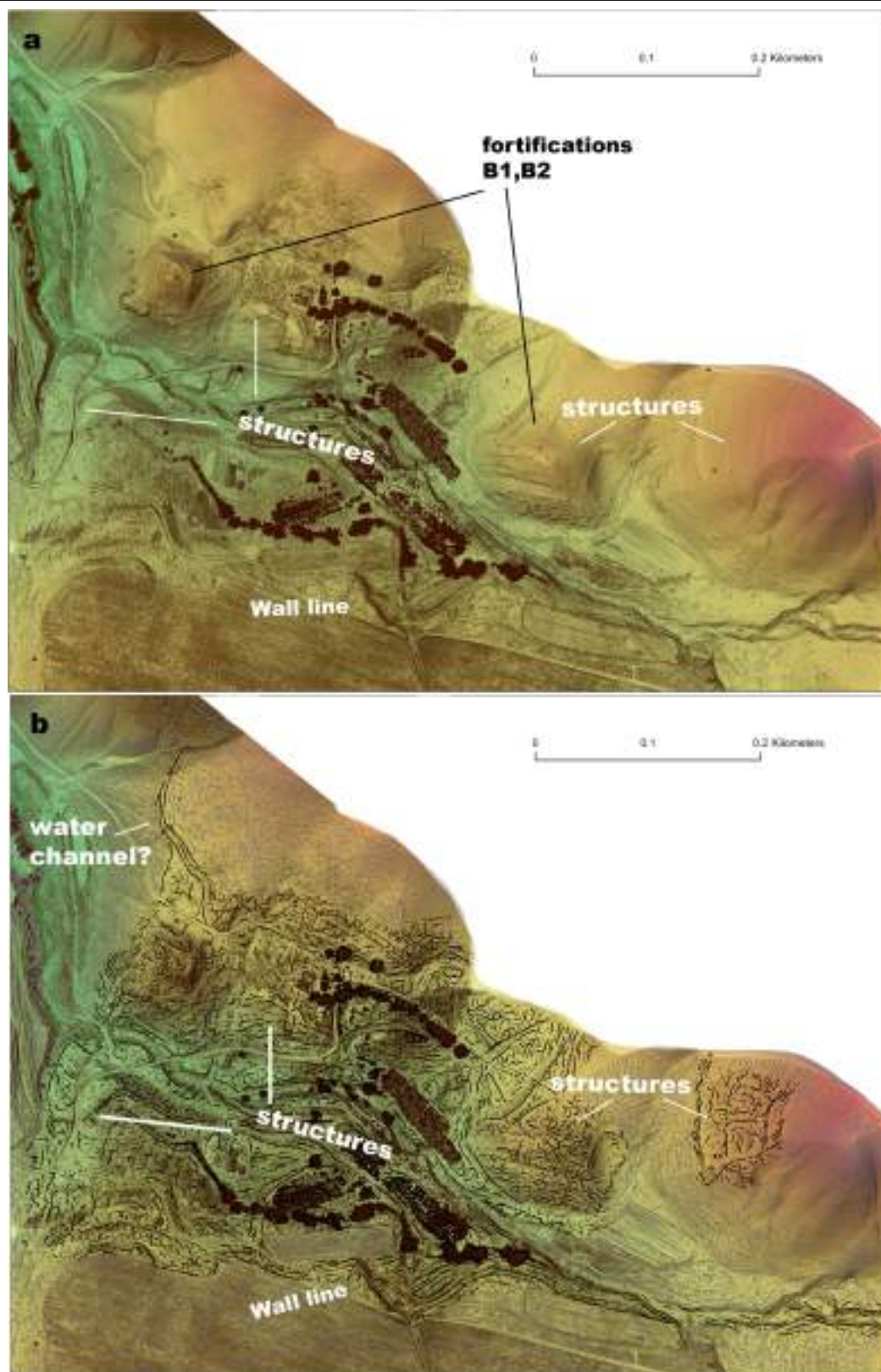
Extended Data Fig. 4 | Lidar and crestline mapping, Tugunbulak sector B. a) Detail of lidar surface of sector B, Tugunbulak (hill-shaded with 2x vertical exaggeration) b) Weighted crest line feature mapping of sector B, Tugunbulak.
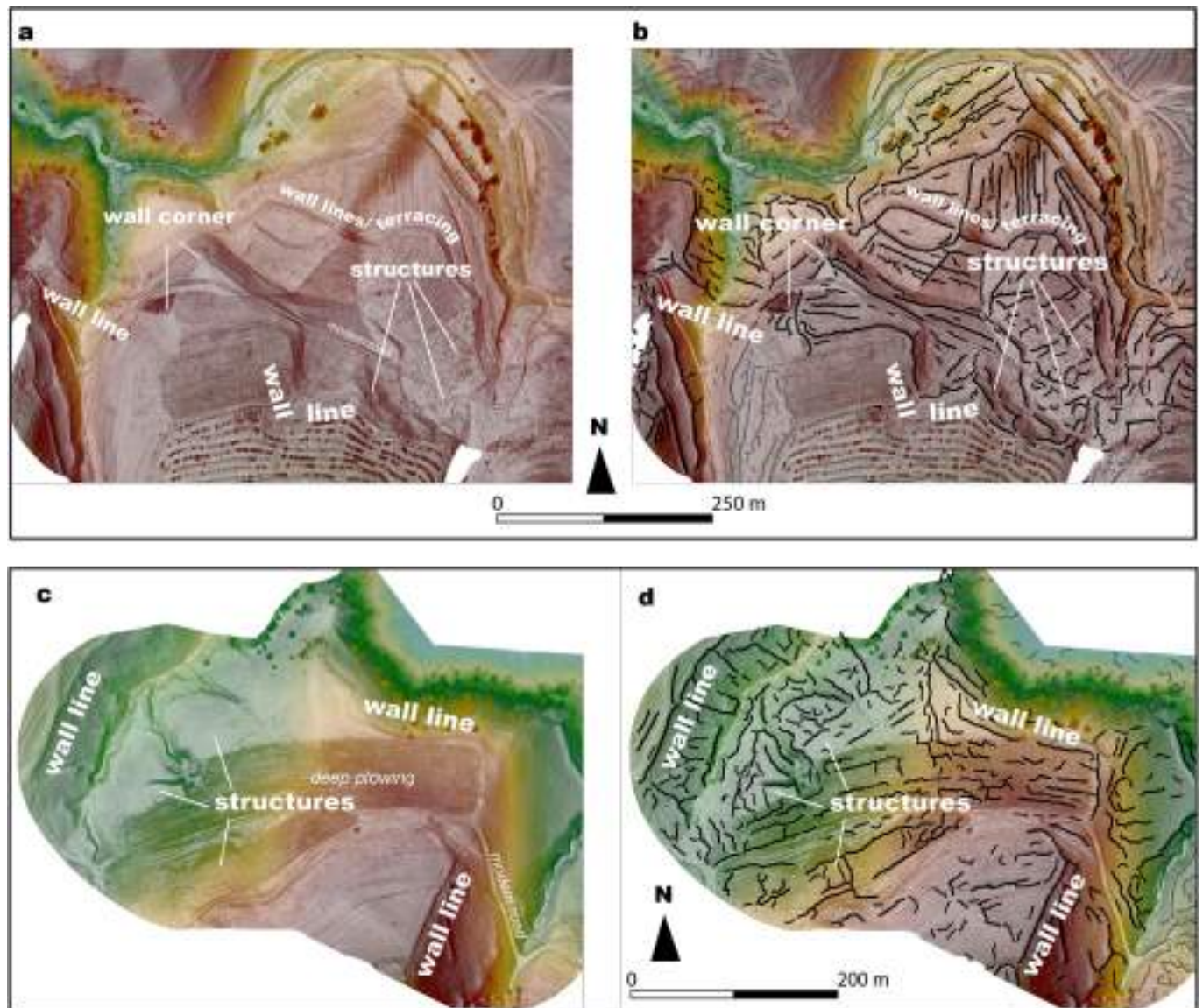
Extended Data Fig. 5 | Lidar and crestline mapping, Tugunbulak sector C and D. a) detail of lidar surface of sector C, Tugunbulak (hill-shaded with 2x vertical exaggeration); b) weighted crest line feature mapping of sector C, Tugunbulak. c) Detailed lidar surface of sector D Tugunbulak (hill-shaded with 2x vertical exaggeration). d) Weighted crest line feature mapping of sector D, Tugunbulak. Note: adjusted parameters for crest line rendering in these images are d = 11 (mesh depth) and n = 4 (neighborhood) (see Methods).

Test area, sector A

Automated Crest line features

Visually identified features

Confusion matrix: radius = .9m

Crest lines intersect with manual lines:

Manual lines intersect with crest lines:

error of omission: 0.191224066
error of commision: 0.777652918
producer accuracy: 0.222347082
User accuracy: 0.808775934
F1: 0.348802162

hit rate: 0.250326513

hit rate: 0.867214488

Confusion matrix: radius = 1.4m

Crest lines intersect with manual lines:

Manual lines intersect with crest lines:

error of omission: 0.053123698
error of commision: 0.672833122
producer accuracy: 0.327166878
User accuracy: 0.946876302
F1: 0.486304654

hit rate: 0.331809607
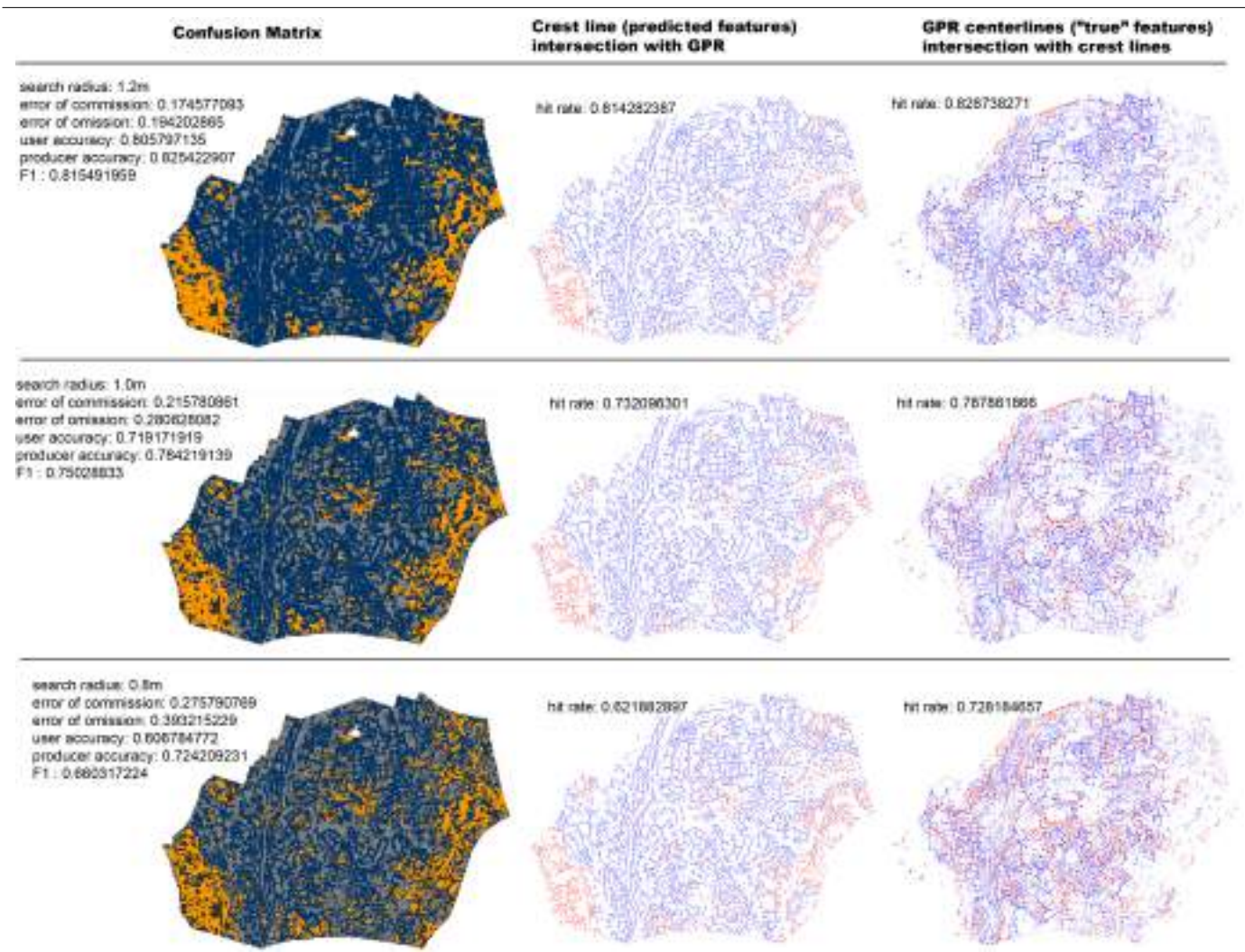
hit rate: 0.979011829

Extended Data Fig. 6 | Correlation and hit rates of Tugunbulak manual tracing and crest lines. Results of confusion matrix and spatial correlation (hit rates) between visually drawn features and semi-auto detected crest lines in selected polygon at Tugunbulak (Blue = hits, Red = miss). Correlation radii shown at .9 m and 1.4 m.

Extended Data Fig. 7 | Correlation and hit rates of Tashbulak GPR and crest lines. Comparative results of confusion matrix and spatial correlation (hit rates) between GPR centerlines and semi-auto detected crest lines in main area of architecture at Tashbulak, (Blue = hits, Red = miss). Correlation radii shown at 0.8 m, 1.0 m and 1.2 m.

Crest lines intersection w/ GPR centerlines

a
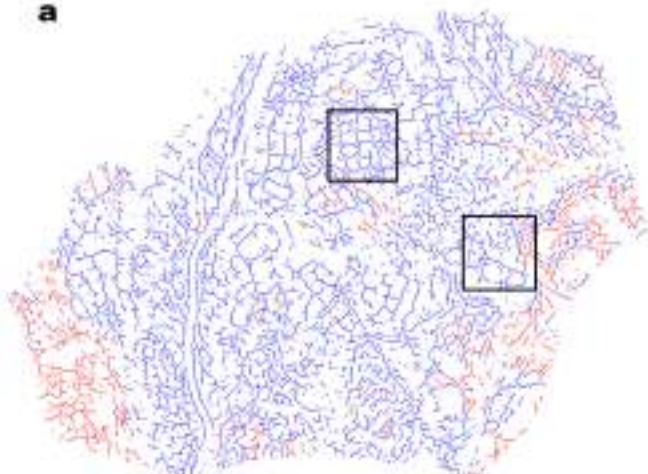
b
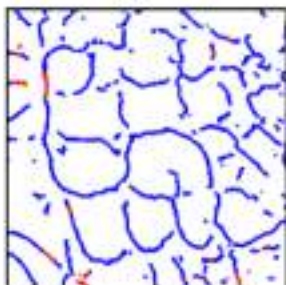
c

GPR centerlines intersection w/ crest lines

d

e

f

Extended Data Fig. 8 | Detailed view, Tashbulak GPR and crestline correlation. Detailed view of correlation between GPR centerlines and semi-auto detected crest lines in two focal areas of architecture at Tashbulak. (Blue = hits, Red = miss). Correlation radius shown at 1.0 m.
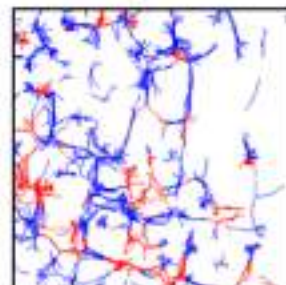
nature portfolio

Corresponding author(s): Frachetti, Michael D

Last updated by author(s): August 24, 2024

Reporting Summary

Nature Portfolio wishes to improve the reproducibility of the work that we publish. This form provides structure for consistency and transparency in reporting. For further information on Nature Portfolio policies, see our Editorial Policies and the Editorial Policy Checklist.

Statistics

For all statistical analyses, confirm that the following items are present in the figure legend, table legend, main text, or Methods section.

n/a	Confirmed	
☐	☒	The exact sample size (*n*) for each experimental group/condition, given as a discrete number and unit of measurement
☐	☒	A statement on whether measurements were taken from distinct samples or whether the same sample was measured repeatedly
☒	☐	The statistical test(s) used AND whether they are one- or two-sided *Only common tests should be described solely by name; describe more complex techniques in the Methods section.*
☒	☐	A description of all covariates tested
☐	☒	A description of any assumptions or corrections, such as tests of normality and adjustment for multiple comparisons
☐	☒	A full description of the statistical parameters including central tendency (e.g. means) or other basic estimates (e.g. regression coefficient) AND variation (e.g. standard deviation) or associated estimates of uncertainty (e.g. confidence intervals)
☒	☐	For null hypothesis testing, the test statistic (e.g. *F*, *t*, *r*) with confidence intervals, effect sizes, degrees of freedom and *P* value noted *Give P values as exact values whenever suitable.*
☒	☐	For Bayesian analysis, information on the choice of priors and Markov chain Monte Carlo settings
☒	☐	For hierarchical and complex designs, identification of the appropriate level for tests and full reporting of outcomes
☒	☐	Estimates of effect sizes (e.g. Cohen's *d*, Pearson's *r*), indicating how they were calculated

Our web collection on statistics for biologists contains articles on many of the points above.

Software and code

Policy information about availability of computer code

Data collection	Lidar data was collected using the GeoSLAM zeb horizon unit mounted to a DJI Matrice 600Pro drone. Raw lidar point clouds were imported and compiled using licensed GeoSLAM connect software (version 2.0).
Data analysis	Individual point cloud files were subsequently georeferenced and co-registered using open source software CloudCompare (CloudCompare v2.12.4). All code and an abridged lidar dataset required to execute crest line analysis and correlation and validation analyses are openly available at the following link: https://github.com/JasonLiu2024/high-resolution-lidar-traces-large-scale-medieval-urbanism

For manuscripts utilizing custom algorithms or software that are central to the research but not yet described in published literature, software must be made available to editors and reviewers. We strongly encourage code deposition in a community repository (e.g. GitHub). See the Nature Portfolio guidelines for submitting code & software for further information.

Data

Policy information about <u>availability of data</u>

All manuscripts must include a <u>data availability statement</u>. This statement should provide the following information, where applicable:

- Accession codes, unique identifiers, or web links for publicly available datasets
- A description of any restrictions on data availability
- For clinical datasets or third party data, please ensure that the statement adheres to our <u>policy</u>

All relevant data are provided with the paper and its online Supplementary Information. The datasets (with accession codes) used to calibrate all radiocarbon dates are available in Supplementary Table 3.

Research involving human participants, their data, or biological material

Policy information about studies with <u>human participants or human data</u>. See also policy information about <u>sex, gender (identity/presentation), and sexual orientation</u> and <u>race, ethnicity and racism</u>.

Reporting on sex and gender	N/A
Reporting on race, ethnicity, or other socially relevant groupings	N/A
Population characteristics	N/A
Recruitment	N/A
Ethics oversight	N/A

Note that full information on the approval of the study protocol must also be provided in the manuscript.

Field-specific reporting

Please select the one below that is the best fit for your research. If you are not sure, read the appropriate sections before making your selection.

☐ Life sciences   ☐ Behavioural & social sciences   ☒ Ecological, evolutionary & environmental sciences

For a reference copy of the document with all sections, see nature.com/documents/nr-reporting-summary-flat.pdf

Ecological, evolutionary & environmental sciences study design

All studies must disclose on these points even when the disclosure is negative.

Study description	This study entailed wide area drone based (UAV) lidar scanning of archaeological sites in Uzbekistan and the use of surface analysis algorithms for the automated delineation of archaeological features (architecture, fortifications, etc).
Research sample	The research 'sample' consisted of 3D point cloud data.
Sampling strategy	Our sampling strategy was to scan a comprehensive territory covering the proposed total spatial extent of the archaeological sites identified.
Data collection	Lidar data was collected from a drone, flown at approximately 30-50m altitude by Michael Frachetti.
Timing and spatial scale	Data was collected in daily fly-overs between June 7-June 22, 2022. All flights were approximately 20-30 minutes, on account of battery power.
Data exclusions	In some cases multiple flights were performed over the same territory, to ensure proper collection and data coverage. for the final analysis, we selected the fewest number of individual scans while preserving adequate spatial overlap between scans for accurate georeferencing and 3D co-registration.
Reproducibility	N/A
Randomization	This is not relevant to this study. By default the data refelct a spatial measurement of topography in high-resolution, so no grouping or co-variation was introduced outside of instrumental conditions.
Blinding	Blinding is not relevant to this study.

Did the study involve field work? ☒ Yes ☐ No

Field work, collection and transport

Field conditions	Field conditions for data collection were rural, high elevation contexts with open terrain.
Location	Zaamin region, Uzbekistan
Access & import/export	Import permission for drone operation was obtained by Governmental Agencies in Uzbekistan. All data was digitally recorded and required no permission for export
Disturbance	No disturbance was created.

Reporting for specific materials, systems and methods

We require information from authors about some types of materials, experimental systems and methods used in many studies. Here, indicate whether each material, system or method listed is relevant to your study. If you are not sure if a list item applies to your research, read the appropriate section before selecting a response.

Materials & experimental systems

n/a	Involved in the study
☒	☐ Antibodies
☒	☐ Eukaryotic cell lines
☐	☒ Palaeontology and archaeology
☒	☐ Animals and other organisms
☒	☐ Clinical data
☒	☐ Dual use research of concern
☒	☐ Plants

Methods

n/a	Involved in the study
☒	☐ ChIP-seq
☒	☐ Flow cytometry
☒	☐ MRI-based neuroimaging

Palaeontology and Archaeology

Specimen provenance	Archaeological specimens for radiocarbon dating were obtained with official permits by the Center for Archaeological Research, Uzbekistan under the joint ARQ project agreement 2022 (PI M Frachetti and F. Maksudov)
Specimen deposition	Sample carbon material is destroyed in the process of AMS analysis.
Dating methods	Organic carbon (charcoal n=5) was collected at the time of excavation and submitted to The UCI Keck Carbon Cycle AMS Program, University of California, Irvine.

☒ Tick this box to confirm that the raw and calibrated dates are available in the paper or in Supplementary Information.

Ethics oversight	No ethical approval was required

Note that full information on the approval of the study protocol must also be provided in the manuscript.

Plants

Seed stocks	N/A
Novel plant genotypes	N/A
Authentication	N/A